Monthly Notices of the ROYAL ASTRONOMICAL SOCIETY

MNRAS **527,** 8103–8117 (2024) https://doi.org/10.1093/mnras/stad3487
Advance Access publication 2023 November 13

In-plane tidal disruption of stars in discs of active galactic nuclei

Taeho Ryu [1,2★] Barry McKernan [3,4,5,6] K. E. Saavik Ford [3,4,5,6] Matteo Cantiello,[3] Matthew Graham [7] Daniel Stern[8] and Nathan W. C. Leigh[4,9]

[1]*Max Planck Institute for Astrophysics, Karl-Schwarzschild-Str. 1, D-85748 Garching, Germany*
[2]*Physics and Astronomy Department, Johns Hopkins University, Baltimore, MD 21218, USA*
[3]*Center for Computational Astrophysics, Flatiron Institute, New York, NY 10010, USA*
[4]*Department of Astrophysics, American Museum of Natural History, New York, NY 10024, USA*
[5]*Graduate Center, City University of New York, 365 5th Avenue, New York, NY 10016, USA*
[6]*Department of Science, BMCC, City University of New York, New York, NY 10007, USA*
[7]*California Institute of Technology, 1200 E. California Blvd, Pasadena, CA 91125, USA*
[8]*Jet Propulsion Laboratory, California Institute of Technology, 4800 Oak Grove Drive, Pasadena, CA 91109, USA*
[9]*Departamento de Astronomá, Facultad de Ciencias Fśicas y Matemáticas, Universidad de Concepción, 4070409 Concepción, Chile*

Accepted 2023 November 4. Received 2023 November 4; in original form 2023 September 30

ABSTRACT

Stars embedded in active galactic nucleus (AGN) discs or captured by them may scatter onto the supermassive black hole (SMBH), leading to a tidal disruption event (TDE). Using the moving-mesh hydrodynamics simulations with AREPO, we investigate the dependence of debris properties in in-plane TDEs in AGN discs on the disc density and the orientation of stellar orbits relative to the disc gas (pro- and retro-grade). Key findings are: (1) Debris experiences continuous perturbations from the disc gas, which can result in significant and continuous changes in debris energy and angular momentum compared to 'naked' TDEs. (2) Above a critical density of a disc around an SMBH with mass $M_\bullet$ [$\rho_{\rm crit} \sim 10^{-8}$ g cm^{-3} $(M_\bullet/10^6\ {\rm M}_\odot)^{-2.5}$] for retrograde stars, both bound and unbound debris is fully mixed into the disc. The density threshold for no bound debris return, inhibiting the accretion component of TDEs, is $\rho_{\rm crit,bound} \sim 10^{-9}$g cm$^{-3}(M_\bullet/10^6\,{\rm M}_\odot)^{-2.5}$. (3) Observationally, AGN-TDEs transition from resembling naked TDEs in the limit of $\rho_{\rm disc} \lesssim 10^{-2}\rho_{\rm crit,bound}$ to fully muffled TDEs with associated inner disc state changes at $\rho_{\rm disc} \gtrsim \rho_{\rm crit,bound}$, with a superposition of AGN + TDE in between. Stellar or remnant passages themselves can significantly perturb the inner disc. This can lead to an immediate X-ray signature and optically detectable inner disc state changes, potentially contributing to the changing-look AGN phenomenon. (4) Debris mixing can enrich the average disc metallicity over time if the star's metallicity exceeds that of the disc gas. We point out that signatures of AGN-TDEs may be found in large AGN surveys.

Key words: accretion, accretion discs – hydrodynamics – galaxies: active – quasars: supermassive black holes – transients: tidal disruption events.

1 INTRODUCTION

Active galactic nuclei (AGN) are powered by the accretion of gas discs onto supermassive black holes (SMBH). The accreting SMBH is often also orbited by a nuclear star cluster (Neumayer, Seth & Böker 2020), which must interact with the gas disc. Depending on the radial size of the gas disc, gas density ($\rho_{\rm disc}$), and how long the disc lasts, some fraction of the nuclear star cluster orbiting the SMBH will be captured by the AGN disc (e.g. Artymowicz, Lin & Wampler 1993; Fabj et al. 2020; Generozov & Perets 2023; Nasim et al. 2023; Wang, Zhu & Lin 2023). Star formation within the AGN disc (e.g. Goodman & Tan 2004; Levin 2007) can also add to the embedded stellar population. Thus, we expect a dynamic population of embedded objects (stars and stellar remnants) to live within AGN discs. The initial population of objects within the AGN disc soon after it forms should consist of both prograde and retrograde orbiters, leading to the possibility of dynamically complex and high-speed encounters and scatterings (e.g. Leigh et al. 2018; Wang et al. 2021). Captured orbiters may include stars on retrograde orbits and high eccentricities at small semimajor axes (Wang, Zhu & Lin 2023). In-plane tidal disruption events in AGN (or simply AGN-TDEs hereafter) can result from either in-plane scatterings of stars onto the SMBH, or eccentricity pumping of stars on retrograde orbits (e.g. Secunda et al. 2021; McKernan et al. 2022). Note that this is *a new source* of TDEs in addition to standard loss-cone filling scattering yielding TDEs at roughly the same rate ($\sim 10^{-4}$ yr^{-1}) as in any other (quiescent) galactic nucleus (e.g. Stone et al. 2020). The loss-cone TDEs (e.g. Hills 1988; Rees 1988) will very likely intersect the AGN disc at an angle and yield a TDE that looks different from a off-plane TDE (Chan, Piran & Krolik 2021).

In-plane AGN TDEs should look more different still. In McKernan et al. (2022) we speculated that AGN-TDEs could look quite different from 'naked' or gas-free TDEs, with observable differences between TDEs that are retrograde or prograde compared to the flow of disc gas. Here we investigate the hydrodynamics of prograde and retrograde

★ E-mail: tryu@mpa-garching.mpg.de

AGN-TDEs using a simple disc model, with a view to qualitatively describing key features of AGN-TDEs and potential observables. Throughout we highlight the point that in-plane AGN TDEs test the dynamics of the disc as well as its embedded population. While stars on prograde orbits embedded in AGN discs may experience runaway mass growth (Cantiello, Jermyn & Lin 2021; Jermyn et al. 2022), we only consider TDEs of normal main-sequence stars.

The paper is organized as follows: we provide descriptions of our numerical methods in detail in Section 2. We present results of our simulations in Section 3 and discuss astrophysical implications in Section 4 and caveats in Section 5. Finally, we conclude with a summary in Section 6.

2 SIMULATION DETAILS

2.1 Numerical methods

We perform 3D hydrodynamic simulations of a tidal disruption event of a main-sequence (MS) star on an in-plane parabolic orbit[1] around an AGN disc surrounding an SMBH, using the massively parallel gravity and magnetohydrodynamic moving-mesh code AREPO (Springel 2010; Pakmor et al. 2016; Weinberger, Springel & Pakmor 2020). It employs a second-order finite-volume scheme to solve the hydrodynamic equations on a moving Voronoi mesh, and a tree-particle-mesh method for gravity calculations. By adopting this innovative approach to grid construction and solving hydrodynamics equations, the code inherits advantages of both commonly used hydrodynamics schemes, Eulerian grid-based methods, and Lagrangian smoothed particle methods. The advantages include improved shock capturing without introducing an artificial viscosity, and adaptive adjustment of spatial resolution.

We use the ideal gas equation $p = (\gamma - 1)u$ with $\gamma = 5/3$, where p is the pressure and u is the gas internal energy density.

2.2 Creation of a star in an AGN disc

To make proper initial conditions for the simulations, we follow several steps, (1) creating a disc (Section 2.2.1), (2) creating a 3D MS star (Section 2.2.2), and (3) placing the star in the disc with a different mid-plane density on a parabolic orbit around an SMBH (Section 2.2.3).

2.2.1 AGN disc around a supermassive black hole

We model the central SMBH using a non-rotating sink particle, which interacts solely through gravitational forces with the gas. We allow the particle to grow in mass via accretion following the same procedure described in Ryu et al. (2023). However, it is worth noting that the total mass accreted remains significantly smaller than the mass of the SMBH throughout the simulation. Consequently, the change in the gravitational potential due to the mass growth of the SMBH would not significantly impact the results presented in this paper.

[1]For naked TDEs, it is a good approximation that a star that is tidally disrupted initially had approached on a parabolic orbit. Even in AGNs, if a star approaches the SMBH from a large distance near the influence radius of the SMBH, the stellar orbit can be approximated as a parabolic orbit. The disc gas would exert a drag force on the star, affecting the orbit. But, in this work, we simply assume a parabolic orbit for simplicity.

For the sake of completeness, we will briefly summarize the adopted accretion prescription. At every time-step, the accretion rate is estimated as an inward radial mass flux towards the BH averaged over cells with weights within $10r_g$ (denoted by 'accretion radius'), and multiplied by the integration area. Here, $r_g = GM_\bullet/c^2$ represents the gravitational radius, which is approximately $2\,R_\odot$ for an SMBH mass of $M_\bullet = 10^6\,M_\odot$. The weights are given using an inverse-distance weighted spline Kernel (Monaghan & Lattanzio 1985) (equation 4 in Springel 2005). If there are only a few cells within the accretion radius, the accretion rate estimate may be affected by Poisson noise. To ensure a sufficient number of cells in proximity to the black hole, we dynamically adjust cell refinement and derefinement within a region slightly larger than the accretion radius, aiming to maintain more than approximately 100 cells within this radius. Specifically, the code refines cells with a density greater than 10^{-14} g cm^{-3} and a mass exceeding 6×10^{22} g, provided that the ratio of the cell size to the distance from the black hole is greater than $\Delta r/r = 0.03$. Conversely, the code derefines cells if their mass falls below 1.5×10^{22} g or if $\Delta r/r < 0.01$.

The thermodynamic profiles of an AGN disc surrounding the SMBH are described by the solution for a gas-pressure dominated disc in Nelson, Gressel & Umurhan (2013). The mid-plane density and temperature follow a power-law in r,

$$\rho_{\rm mid}(r) = \rho_{\rm c}\left(\frac{r}{r_{\rm cusp}}\right)^{p}, \tag{1}$$

$$T_{\rm mid}(r) = T_{\rm c}\left(\frac{r}{r_{\rm cusp}}\right)^{q}, \tag{2}$$

where $\rho_{\rm c}$ and $T_{\rm c}$ are the mid-plane density and temperature near the inner edge of the disc, respectively, and $r_{\rm cusp} = 10^3 r_g$. In this work, we consider a disc surrounding a $10^6\,M_\odot$ SMBH with the mid-plane density $\rho_{\rm c} = 10^{-7}$–10^{-12} g cm^{-3} at the inner disc edge $R_{\rm inner} = 100r_g$. To match the disc solution by Sirko & Goodman (2003), we adopt the values of p,

$$p = \begin{cases} 0 & \text{for } r < r_{\rm cusp} \\ -3 & \text{for } r > r_{\rm cusp}, \end{cases} \tag{3}$$

and $q = -3/4$.

The vertical structure, i.e. the density and angular frequency Ω, of the disc is described by the following equations,

$$\rho_{\rm disc}(r,z) = \rho_{\rm mid}(r)\exp\left(\left[\tfrac{h}{r}\right]^{-2}\left[\frac{1}{\sqrt{1+(z/r)^2}} - 1\right]\right), \tag{4}$$

$$\Omega_{\rm disc}(r,z) = \Omega_{\rm K}\left[(p+q)\left(\tfrac{h}{r}\right)^2 + (1+q) - \frac{q}{\sqrt{1+(z/r)^2}}\right]^{1/2}, \tag{5}$$

where $\Omega_{\rm K} = \sqrt{GM_\bullet/r^3}$ is the Keplerian angular frequency and h/r the aspect ratio. Note that the temperature has no dependence on the vertical distance orthogonal to the mid-plane z, meaning the temperature (so the sound speed) is constant along each vertical column at given r.

The disc is fully described if $\rho_{\rm c}$, $T_{\rm c}$, and h/r at $R_{\rm inner}$ are determined. For a given $\rho_{\rm c}$ we estimate the two other disc parameters using the following equations from Sirko & Goodman (2003),

$$c_{\rm s}^2\Sigma = \tfrac{\dot{M}'\Omega}{3\pi\alpha}, \tag{6}$$

$$\Sigma = 2\rho_{\rm c}h, \tag{7}$$

$$h = \tfrac{c_{\rm s}}{\Omega}, \tag{8}$$

where $\dot{M}' = \dot{M}(1 - \sqrt{\frac{5r_g}{R_{\rm inner}}})$ and $\dot{M}$ is the accretion rate. Assuming $\dot{M} = 0.5\dot{M}_{\rm Edd}$, $\dot{M}' \simeq 0.4\dot{M}_{\rm Edd}$ at $R_{\rm inner} = 100r_g$. Here,

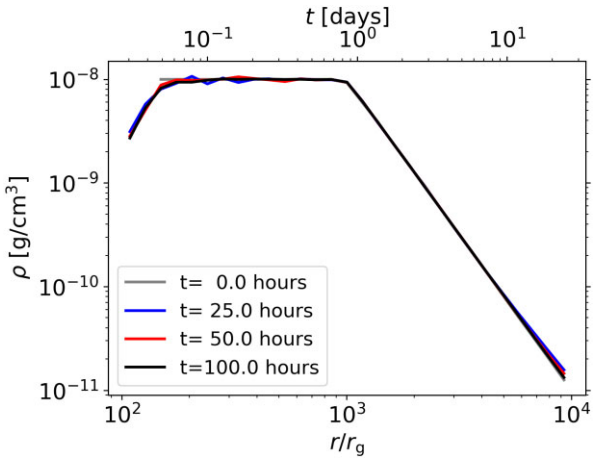

Figure 1. Average mid-plane density of our fiducial AGN disc model at four different times: $t = 0$ h (grey dotted), 25 h (blue solid), 50 h (red solid), 100 h (black solid). The upper x-axis indicates the time which it takes for a star on a parabolic orbit to reach the given distance.Co

$\dot{M}_{\rm Edd} = 10 L_{\rm Edd}/c^2$ where $L_{\rm Edd}$ is the Eddington luminosity and a radiation efficiency of $\eta = 0.1$ is assumed. And $\alpha = 0.01$ is the viscosity parameter. Combining equations (6), (7), and (8), we find an expression for h/r,

$$\frac{h}{r} = \left(\frac{\dot{M}'}{6\pi\alpha\rho_{\rm c}\Omega}\right)^{1/3} r^{-1}. \tag{9}$$

Once h/r is estimated, equation (8) determines $T_{\rm c}$ from the assumed ideal equation of state.

Using the disc solution, we construct a disc extending out to $\simeq 10^4 r_{\rm g}$ for $M_\bullet = 10^6\,{\rm M}_\odot$, corresponding to $2 \times 10^4\,{\rm R}_\odot$, using $\simeq 10^7$ cells. Fig. 1 shows the mid-plane density of a fully relaxed disc in our fiducial model ($\rho_{\rm c} = 10^{-8}\,{\rm g\,cm^{-3}}$) while Fig. 2 depicts the mid-plane density and enclosed mass of fully relaxed discs with a different $\rho_{\rm c}$. The disc parameters for our models are summarized in Table 1.

2.2.2 *Stellar model*

The initial state of the star in our hydrodynamics simulations was taken from stellar models evolved using the stellar evolution code MESA (version r22.05.1) (Paxton et al. 2011, 2013, 2015, 2019; Jermyn et al. 2023). We consider MS stars with three different masses, $M_\star = 1$, 3, and $10\,{\rm M}_\odot$, when the core H mass fraction is 0.3. The stellar radii of those stars are $R_\star = 0.95$, 2.5, and $4.7\,{\rm R}_\odot$, respectively. Stars can grow in mass via accretion in the AGN discs (Cantiello, Jermyn & Lin 2021). The rate of accretion significantly influences the internal structure and chemical compositions of stars embedded in the disc. However, for those stars which approach the SMBH on a parabolic orbit from the effective radius of the nuclear cluster, $\simeq 0.5\,{\rm pc} \simeq 10^7 r_{\rm g}$ for $M_\bullet = 10^6\,{\rm M}_\odot$ (Neumayer, Seth & Böker 2020), and are disrupted at the first pericentre passage, the accretion onto the star would not be significant. Assuming a Bondi–Hoyle accretion (Bondi & Hoyle 1944; Bondi 1952)[2] onto a $1\,{\rm M}_\odot$ star on a parabolic orbit in our disc with $\rho_{\rm c} = 10^{-8}\,{\rm g\,cm^{-3}}$, the accretion rate can be estimated as $\dot{M} \simeq 10^{-15}\,{\rm M}_\odot\,{\rm yr}^{-1}(r/10^7 r_{\rm g})^{-3/2}$. The total accreted mass until the star reaches the SMBH is $\simeq 10^{-10}\,{\rm M}_\odot$.

[2]The Bondi radius $\propto 1/[c_{\rm s}^2 + v^2] \propto v^{-2}$ where v is the speed of the star because $c_{\rm s} \lesssim v$.

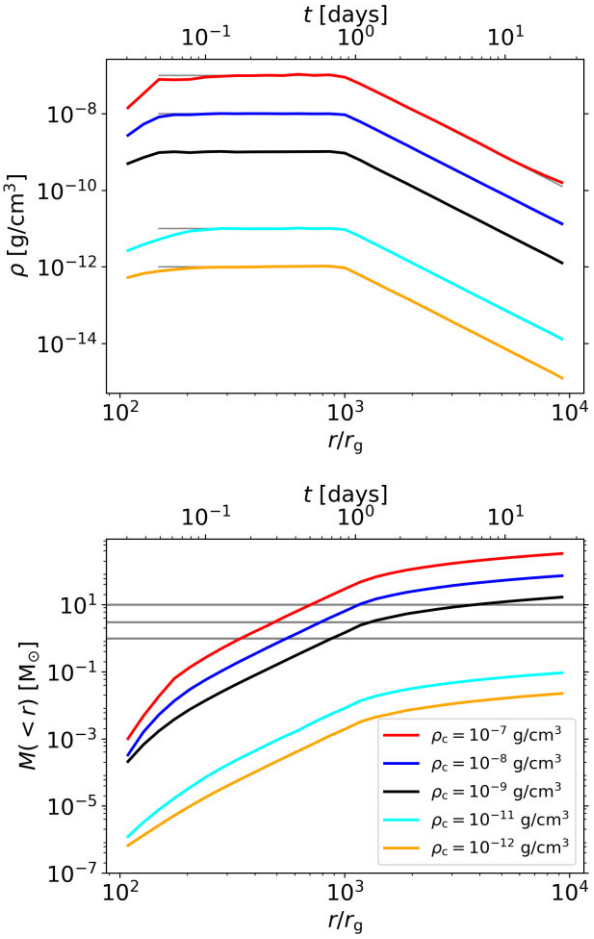

Figure 2. Mid-plane density (top) and enclosed mass (bottom) of fully relaxed discs with a different initial mid-plane density. The grey lines in the top panel showing the initial density profile are just sitting on top of the profile for the relaxed discs. On the other hand, the grey horizontal lines in the bottom panel indicate the masses of the stars considered. Like Fig. 1, the upper x-axis shows how long it takes for a star on a parabolic orbit to travel the given distance.

Table 1. Disc parameters: (*first*) black hole mass $M_\bullet$, (*second*) assumed mass accretion rate $\dot{M}$ relative to the Eddington mass accretion rate $M_{\rm Edd}$, (*third*) maximum density in the mid-plane $\rho_{\rm c}$ (see equation 1), (*fourth*) maximum temperature in the mid-plane $T_{\rm c}$ (see equation 2), and (*fifth*) aspect ratio at $r = R_{\rm inner}$.

$M_\bullet$ ($\rm M_\odot$)	$\dot{M}/\dot{M}_{\rm Edd}$	$\rho_{\rm c}$ (g/cm^{-3})	$T_{\rm c}$ (K)	$h/r(r = R_{\rm inner})$
10^6	0.5	10^{-7}	8×10^7	0.04
10^6	0.5	10^{-8}	4×10^8	0.08
10^6	0.5	10^{-9}	2×10^9	0.16
10^6	0.001	10^{-11}	6×10^8	0.10
10^6	0.001	10^{-12}	3×10^9	0.21

Going one step further, because the dynamical friction is $\propto \dot{M} v$ (Lee & Stahler 2011, 2014) where v is the speed of the star, the total momentum of disc gas interacting with the star is many orders of magnitude smaller than the angular momentum of the stellar orbit.

We first map the 1D MESA model into a 3D AREPO grid with $N \simeq 10^6$ cells using the mapping routine by Ohlmann et al. (2017). Then we fully relax the 3D single star, which usually takes up to five stellar dynamical times $\sqrt{R_\star^3/GM_\star}$. Fig. 3 depicts the radial

Table 2. Initial parameters: (left to right) model number, black hole mass $M_\bullet(\mathrm{M}_\odot)$, stellar mass $M_\star(\mathrm{M}_\odot)$, maximum mid-plane density ρ_c, relative orientation (prograde versus retrograde), pericentre distance r_p measured in units of the tidal radius r_t, r_p measured in units of the gravitational radius r_g, dynamical time t_p at pericentre.

Model number	$M_\bullet$ ($\mathrm{M}_\odot$)	$M_\star$ ($\mathrm{M}_\odot$)	ρ_c (g/cm^{-3})	Pro. or retro.	r_p/r_t	$r_p[r_g]$	t_p (h)
1	10^6	1	10^{-7}	Pro	0.3	13	0.07
2	10^6	1	10^{-7}	Retro	0.3	13	0.07
3	10^6	1	10^{-8}	Pro	0.3	13	0.07
4	10^6	1	10^{-8}	Retro	0.3	13	0.07
5	10^6	1	10^{-9}	Pro	0.3	13	0.07
6	10^6	1	10^{-9}	Retro	0.3	13	0.07
7	10^6	1	10^{-11}	Pro	0.3	13	0.07
8	10^6	1	10^{-11}	Retro	0.3	13	0.07
9	10^6	1	10^{-12}	Pro	0.3	13	0.07
10	10^6	1	10^{-12}	Retro	0.3	13	0.07
11	10^6	3	10^{-8}	Pro	0.3	24	0.15
12	10^6	3	10^{-8}	Retro	0.3	24	0.15
13	10^6	10	10^{-8}	Pro	0.3	30	0.22
14	10^6	10	10^{-8}	Retro	0.3	30	0.22

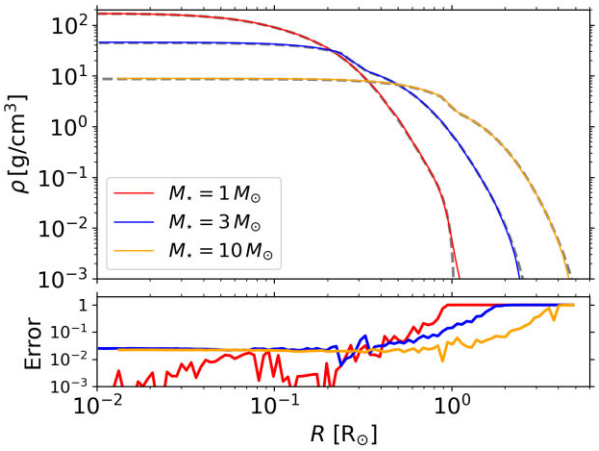

Figure 3. Radial density (top) of fully relaxed 3D stars with mass $M_\star = 1\,\mathrm{M}_\odot$ (red solid), $3\,\mathrm{M}_\odot$ (blue solid), and $10\,\mathrm{M}_\odot$ (orange solid), over-plotted with lines for the MESA models (grey dashed lines) and the relative errors (bottom) between the two density profiles.

density profile of the fully relaxed stars in comparison with the MESA models. The internal profile of the 3D star matches the MESA model within less than a few per cent except near the surface, corresponding to only a few per cent of the total mass, where the error is greater than 10 per cent.

2.2.3 *Initial conditions for star + disc model*

The relaxed stars are initially placed at $8r_t$ on a parabolic orbit with a pericentre distance $r_p \simeq 0.3r_t$ where r_t is the tidal disruption radius, defined as $r_t \equiv (M_\bullet/M_\star)^{1/3} R_\star$. The pericentre distance was chosen to ensure a complete disruption of the star in our fiducial model while keeping the events from becoming too relativistic. We consider both prograde and retrograde orbits of the star relative to the orbit of the disc. Our fiducial models assume $\rho_c = 10^{-8}\,\mathrm{g\,cm^{-3}}$. In addition, we consider $\rho_c = 10^{-7}$, 10^{-9}, 10^{-11}, and $10^{-12}\,\mathrm{g\,cm^{-3}}$. For reference, we perform the simulation of a TDE in an extremely low-density medium with $\rho \simeq 10^{-20}\,\mathrm{g\,cm^{-3}}$, representing a vacuum, sharing the same encounter parameters of our fiducial model. To examine the stellar-mass dependence, we examine the post-disruption properties of the disc and debris for stars with $M_\star = 3$ and $10\,\mathrm{M}_\odot$. For these cases, we only consider $\rho_c = 10^{-8}\,\mathrm{g\,cm^{-3}}$.

We performed convergence tests for the retrograde version of our fiducial models with different resolutions for the star ($N_\star = 125\,000$, $250\,000$, $500\,000$, 10^6 cells) and disc ($N_{\rm disc} = 6 \times 10^6$ and 1.2×10^7). By comparing several key quantities (e.g. debris mass as a function of radius from the black hole, the average radial mass infall rate towards the black hole), we confirmed that the results have already converged very well with $N_\star = 250\,000$ and $N_{\rm disc} = 6 \times 10^6$. To ensure the convergence, we chose $N_\star = 10^6$.

We summarize the model parameters in Table 2.

3 RESULTS

3.1 Overview

We first provide a qualitative overview of the results of our simulations. More quantitative descriptions will be given in the following sections.

Fig. 4 shows successive moments in a full disruption of the $1\,\mathrm{M}_\odot$ star in our fiducial models ($\rho_c = 10^{-8}\,\mathrm{g\,cm^{-3}}$) with a prograde (*left*) and retrograde (*right*) orbit. For comparison, we show in the *middle* column the same moments in a naked TDE sharing the same encounter parameters. The pre-disruption orbit and the internal structure of the star are not significantly affected by the disc provided a negligible amount of disc mass is interacting with the star until it reaches pericentre (*1st* panels). Upon disruption, the debris starts to expand in size. The increasingly larger cross-sections make the debris more subject to interacting with the disc (*2nd* − *3rd* panels). Depending on whether the orbit is prograde or retrograde, the evolution of the debris can be qualitatively different, meaning potentially different observational signatures.

In the prograde case, the outer edges of the debris are gradually mixed into the disc via the Rayleigh–Taylor instability (Rayleigh 1882; Taylor 1950). Due to the coherent motion between the debris and disc, as illustrated in the *left* panel of Fig. 5, the interaction with the disc acts to add angular momentum to the debris. On the other hand, the evolution of debris in the retrograde case is more dramatic due to the significant cancellation of angular momentum. In the retrograde case, like the prograde case, the debris is continuously lost to the disc. But the mixing is more violent, which is shown in the

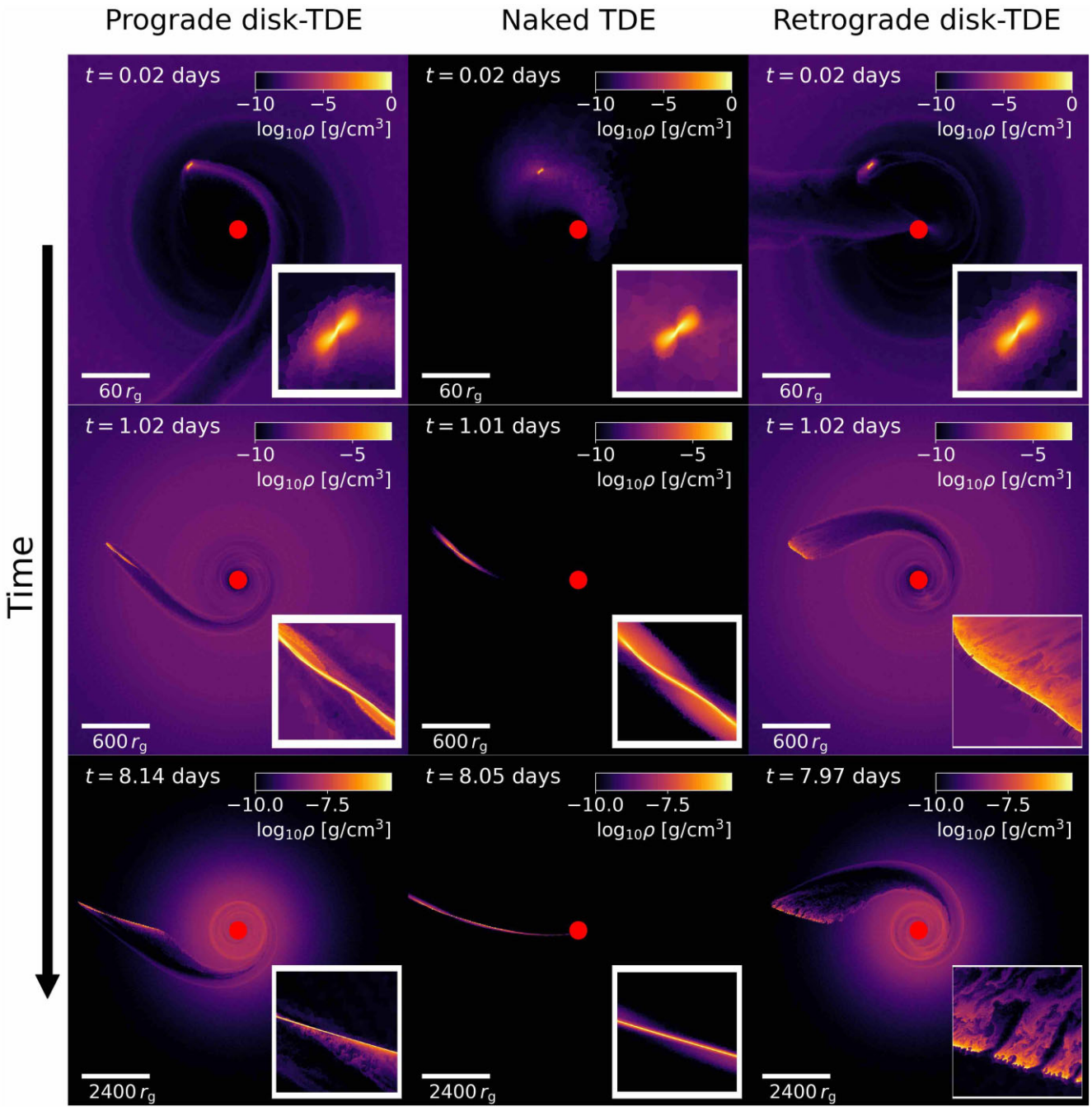

Figure 4. Successive moments in a full disruption event in a prograde (left) and retrograde (right) disc with a mid-plane density of $\rho_c = 10^{-8}$ g cm^{-3}. The middle column shows them in a naked disruption event at the same times. The spatial scale shown in the inset corresponds to roughly 1/20 of the size indicated below the bar on the left-bottom corner. Continuous interactions between the debris and the disc gas result in a significant perturbation of the debris's orbit and, therefore, its structure. The impact of the disc interaction is greater for the retrograde orbit than the prograde orbit. At later times, the debris is completely disintegrated and mixed into the disc.

3rd right panel of Fig. 5. As a result, the initially coherent motion of the debris is significantly perturbed even before any of the bound matter starts to return to the SMBH. Because of increasingly irregular perturbations caused by the Rayleigh–Taylor instability, the energy distribution and the resulting fallback curve of the debris tend to be bumpier than that for the prograde case. In the case of a sufficiently high mid-plane density (e.g. $\rho_c = 10^{-8}$ g cm^{-3}), the entire debris can be mixed with the disc in less time than the peak fallback time of debris in a naked TDE with the same disruption parameters.

3.2 Debris mass-loss – semi-analytic approach

To quantify the mass-loss of debris to the disc, we distinguish the debris from the disc gas using a passive scalar. The passive scalar is an artificial scalar quantity initially assigned to each cell. The scalar then evolves via advection. The initial value of the passive scalar for the cells that belong to the stars is one, and for the disc cells, it is zero. Depending on the mass exchange (and thus momentum exchange) between the cells, the passive scalar varies between zero (for disc

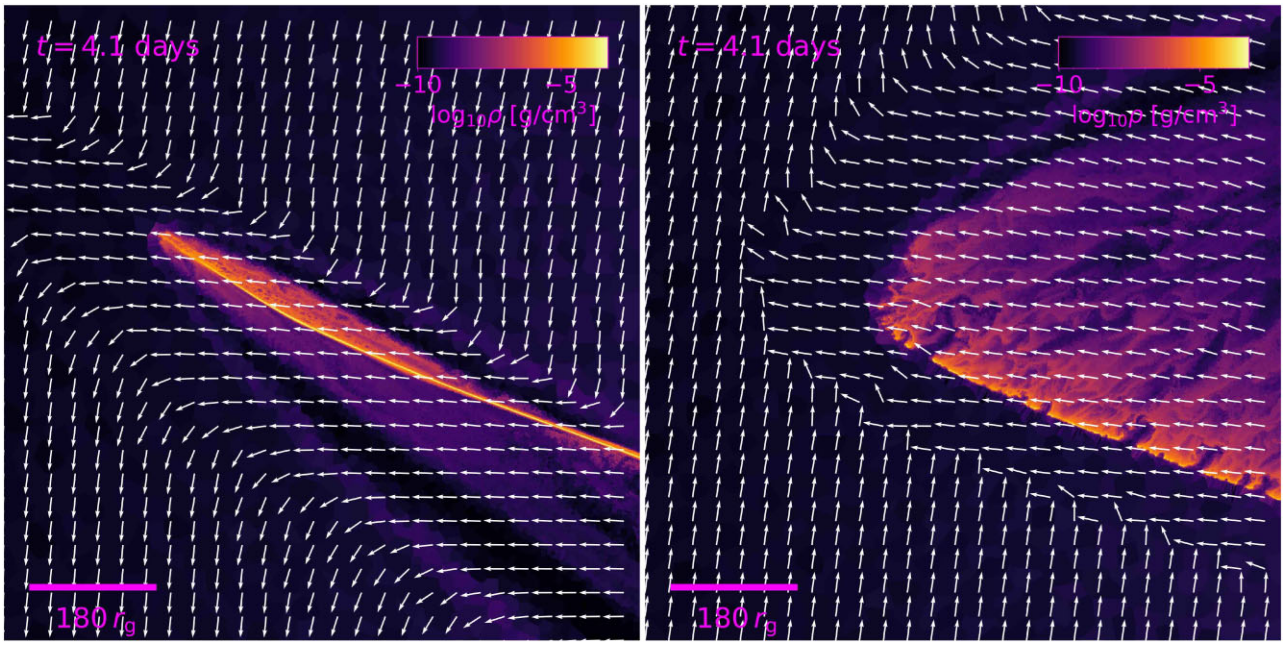

Figure 5. Zoom-in near the head of the debris for the prograde (left) and retrograde (right) cases with $\rho_c = 10^{-8}\,\mathrm{g\,cm^{-3}}$, measured at ∼4 d after disruption. The white arrows show the direction of motion of the gas. In the prograde case, the disc interactions act to increase the angular momentum of the debris whereas, in the retrograde case, the disc interactions cancel out the angular momentum of the debris.

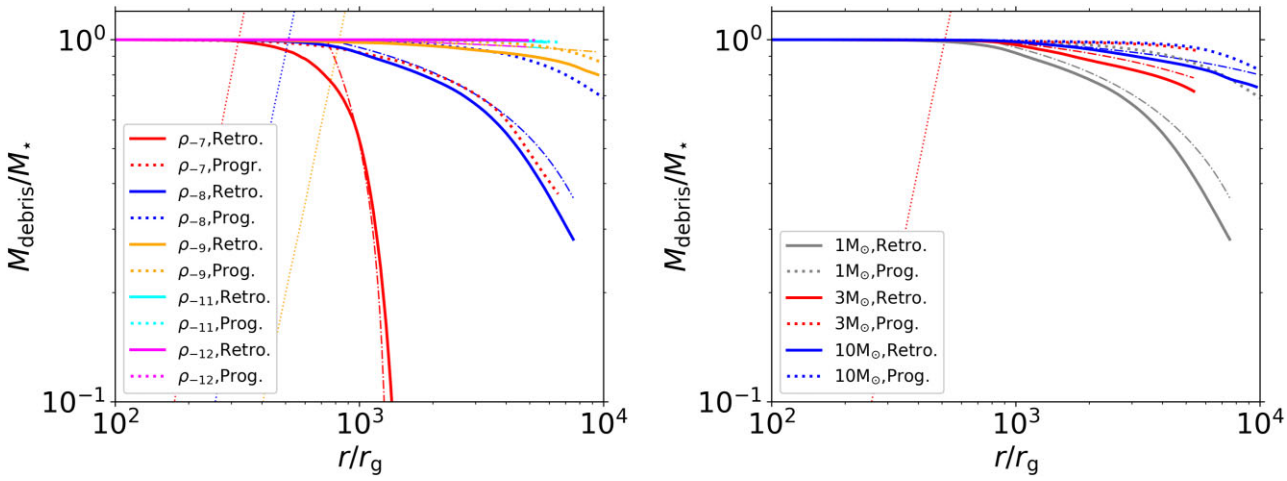

Figure 6. Time evolution of the fractional remaining debris mass that has not been mixed into the disc as a function of the distance of the centre of mass of the debris from the black hole for different models: (left) different disc densities and (right) different stellar masses. The solid (dotted) lines represent the prograde (retrograde) cases. The dot–dashed diagonal lines in both panels indicate the prediction from our semi-analytic model for the retrograde cases (Section 3.2). The dotted diagonal lines show the enclosed mass of the disc: in the left panel, the colours of the lines for the disc enclosed mass match those for the debris mass while in the right panel, the disc mass is for $\rho_c = 10^{-8}\,\mathrm{g\,cm^{-3}}$.

cells) and one (for cells originally in the stars). Identifying a specific region of gas with a passive scalar has been used in the literature to investigate mixing of gas in various contexts (e.g. McCourt et al. 2015; Gronke & Oh 2018; Dutta & Sharma 2019; Kanjilal, Dutta & Sharma 2021; Farber & Gronke 2022; Farber et al. 2022). Our close investigation of the distribution of the scalar suggests that the scalar quantity for the debris in a coherent motion is generally larger than 0.99, meaning it mixes with the disc material by roughly less than 1 per cent in mass.

Fig. 6 illustrates the fractional mass of debris relative to the initial stellar mass as a function of the distance of the centre of mass of debris from the SMBH. The *left* (*right*) panel compares the debris mass between models with different mid-plane disc densities (stellar masses). The most noticeable difference is between the prograde and retrograde cases. For the case with the retrograde orbit relative to the disc with the highest density ($\rho_c = 10^{-7}\,\mathrm{g\,cm^{-3}}$, red solid line in the *left* panel), the entire debris gets mixed to the disc near the density cusp at $r \simeq 10^3 r_g$. On the other hand, for the prograde case with the same disc, the mass-loss is less severe: $\simeq 30$ per cent of the debris survives until it reaches $7000 r_g$. As the disc mid-plane density decreases or the stellar mass increases, a larger fraction of debris can reach farther out.

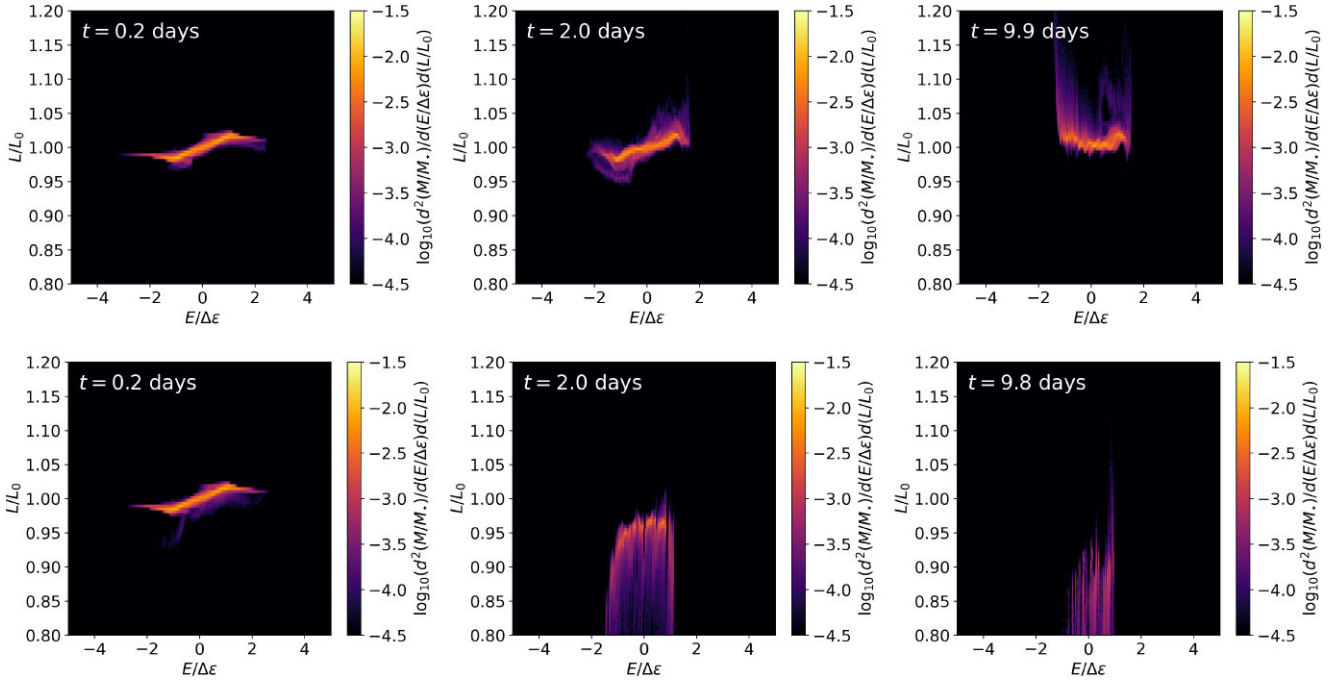

Figure 7. Distribution of specific energy E and specific angular momentum L for a full disruption of a 1 $M_\odot$ star on a prograde (top) and retrograde (bottom) orbit relative to that of a disc with $\rho_c = 10^{-8}$ g cm^{-3} around a 10^6 $M_\odot$ SMBH at three different times.

The impact of the debris mass-loss on the disc structure would be insignificant because the enclosed mass of the disc (dotted diagonal lines in Fig. 6) is many orders of magnitude greater than the stellar mass by the time the entire debris is dissociated and mixed into the disc.

We can understand the trends of debris mass-loss to the disc by comparing how much disc mass interacts to remove the momentum of the debris along the way out. To this end, we build a semi-analytic model for the mass of debris that is mixed to the disc in the retrograde case, which allows us to estimate the maximum distance that the debris can travel through a disc. For the prograde case, the momentum of the disc is added to the debris (see Fig. 7), so this semi-analytic model would not apply to the prograde case.

We assume that the disruption of the coherent motion of the debris is primarily governed by the amount of mass of the disc flow hitting the debris. In other words, the remaining debris mass $M_{\rm debris}$ that continues to follow the orbit that the debris would have assuming a ballistic orbit is simply the initial debris mass or stellar mass $M_\star$ minus the mass of disc flow $M_{\rm d}$ continuously interacting with the debris,

$$M_{\rm debris}(t) = M_\star - M_{\rm d}(t). \tag{10}$$

When the self-gravity is not important, the slow-down of the debris would naturally lead to mixing into the disc. However, when the self-gravity is strong, the entire debris would slow down instead of mixing into the disc. The former is more relevant for AGN-TDEs.

We may be able to estimate $M_{\rm d}(t)$ as,

$$M_{\rm d}(t) \sim \int_0^t \rho_{\rm disc}(r) v_{\rm disc}(r) A_{\rm debris}(t') {\rm d}t', \tag{11}$$

where $\rho_{\rm disc}(r)$ is the density at distance r from the SMBH, $v_{\rm disc}(r) \simeq \sqrt{GM_\bullet/r}$ the flow speed at r, and $A_{\rm debris}$ the cross-section of the debris whose normal is parallel to the disc flow. Although each part of the debris moves at a different speed, we simply assume that the entire debris continues to follow the original orbit of the star, i.e. parabolic orbit, so that $r(t)$ since disruption is expressed,

$$r(t) = \left(\frac{9GM_\bullet}{2}\right)^{1/3} t^{2/3}, \tag{12}$$

and the radial velocity is,

$$v_{\rm debris}(t) = \frac{{\rm d}r(t)}{{\rm d}t} = \frac{2}{3}\left(\frac{9GM_\bullet}{2}\right)^{1/3} t^{-1/3}. \tag{13}$$

With equations (12) and (13), $\rho_{\rm disc}(r)$ and $v_{\rm disc}(r)$ are now a function of time. To calculate $A_{\rm debris}(t)$, we assume that by the time the debris arrives at $r \simeq r_{\rm t}$ since disruption, the debris extends to $l_{\rm debris} \simeq \alpha R_\star$ with a width $w \simeq R_\star$, where $\alpha \simeq$ 20–22 from our simulations (see Fig. 4). We further assume that the debris expands in size such that $l \propto t^{4/3}$ and $w_{\rm debris} \propto t^{1/3}$ before the most bound debris starts to return (Coughlin et al. 2016; Bonnerot & Stone 2021). These assumptions allow us to write an expression for $l_{\rm debris}$ and $w_{\rm debris}$,

$$\begin{aligned} l_{\rm debris} &\simeq \alpha\ R_\star \left(\frac{t}{t(r=r_{\rm t})}\right)^{4/3}, \\ &\simeq \alpha\, {\rm R}_\odot \left(\frac{M_\star}{1\,{\rm M}_\odot}\right)^{2/3} \left(\frac{R_\star}{1\,{\rm R}_\odot}\right)^{-1} \left(\frac{t}{0.01\,{\rm d}}\right)^{4/3}, \end{aligned} \tag{14}$$

and

$$\begin{aligned} w_{\rm debris} &\simeq\ R_\star \left(\frac{t}{t(r=r_{\rm t})}\right)^{1/3}, \\ &\simeq {\rm R}_\odot \left(\frac{M_\star}{1\,{\rm M}_\odot}\right)^{1/6} \left(\frac{R_\star}{1\,{\rm R}_\odot}\right)^{1/2} \left(\frac{t}{0.01\,{\rm d}}\right)^{1/3}, \end{aligned} \tag{15}$$

where $t(r = r_{\rm t})$ is estimated using equation (12). Note that the average density of debris $\bar{\rho}_{\rm debris} \propto M_\star/[l_{\rm debris} h^2_{\rm debris}] \propto t^{-2}$, which we have confirmed from our simulations. It follows that the cross-section $A_{\rm debris}$ is,

$$A_{\rm debris} \simeq l_{\rm debris} w_{\rm debris} \simeq \alpha\, {\rm R}_\odot^2 \left(\frac{M_\star}{1\,{\rm M}_\odot}\right)^{5/6} \left(\frac{R_\star}{1\,{\rm R}_\odot}\right)^{-1/2} \left(\frac{t}{0.01\,{\rm d}}\right)^{5/3}. \tag{16}$$

Because the disc density profile has two regions, i.e. flat for $r < r_{\rm cusp} = 10^3 r_{\rm g}$ and power law for $r > r_{\rm cusp}$, we will calculate the mass-loss due to disc-debris interaction for the two regions separately.

(i) *Flat region ($\rho_{disc} = \rho_c$)*: the time required for the debris to reach the cusp is roughly estimated using equation (12),

$$t_{\rm cusp} = t(r = r_{\rm cusp}) \simeq 0.85\,{\rm d} \left(\frac{r_{\rm cusp}}{10^3 r_{\rm g}}\right)^{3/2} \left(\frac{M_\bullet}{10^6\,{\rm M}_\odot}\right)^{-1/2}. \quad (17)$$

So for $t < t_{\rm cusp}$, the mass-loss is,

$$\begin{aligned} M_{\rm d}^{r<r_{\rm cusp}}(t) &\simeq \int_0^t \rho_{\rm c} v_{\rm disc}(r(t')) A_{\rm debris}(t') {\rm d}t', \\ &= 0.05\,{\rm M}_\odot \left(\frac{\alpha}{22}\right) \left(\frac{M_\bullet}{10^6\,{\rm M}_\odot}\right)^{1/3} \left(\frac{M_\star}{1\,{\rm M}_\odot}\right)^{5/6} \left(\frac{R_\star}{1\,{\rm R}_\odot}\right)^{-1/2} \\ &\times \left(\frac{\rho_{\rm c}}{10^{-8}\ {\rm g\ cm^{-3}}}\right) \left(\frac{t}{0.85\,{\rm d}}\right)^{7/3}. \end{aligned} \quad (18)$$

As shown in the equation, the fractional mass-loss $M_{\rm d}^{r<r_{\rm cusp}}/M_\star$ has a relatively weak dependence on $M_\star$ ($\propto M_\star^{-1/6}$) and $M_\bullet$ ($\propto M_\bullet^{1/3}$), but rather strongly depends on $\rho_{\rm c}$. For example, roughly half the debris mass would be mixed to the disc at $r \simeq r_{\rm cusp}$ (or $t \simeq 0.85$ d) when $\rho_{\rm c} \simeq 10^{-7}\,{\rm g\,cm^{-3}}$, which is illustrated in the *left* panel (red solid line) of Fig. 6.

(ii) *Power-law region ($\rho_{disc} \propto r^p$ with $p = -3$)*: the mass-loss at $t_{\rm cusp} \lesssim t \lesssim t_0$ is,

$$\begin{aligned} &M_{\rm d}^{r>r_{\rm cusp}}(t) \\ &\simeq M_{\rm d}^{r<r_{\rm cusp}}(t = t_{\rm cusp}) + \int_{t_{\rm cusp}}^t \rho_{\rm c} \left(\frac{r(t')}{r_{\rm cusp}}\right)^{-3} v_{\rm disc}(r(t')) A_{\rm debris}(t') {\rm d}t', \\ &= \left(\frac{\alpha}{22}\right) \left(\frac{M_\bullet}{10^6\,{\rm M}_\odot}\right)^{-2/3} \left(\frac{M_\star}{1\,{\rm M}_\odot}\right)^{5/6} \\ &\times \left(\frac{R_\star}{1\,{\rm R}_\odot}\right)^{-1/2} \left(\frac{r_{\rm cusp}}{10^3 r_{\rm g}}\right)^3 \left(\frac{\rho_{\rm c}}{10^{-8}\ {\rm g\ cm^{-3}}}\right) \\ &\times \left[-0.3\,{\rm M}_\odot \left(\frac{r_{\rm cusp}}{10^3 r_{\rm g}}\right)^{1/2} \left(\frac{M_\bullet}{10^6\,{\rm M}_\odot}\right)^{-1/6} + 0.85\,{\rm M}_\odot \left(\frac{t}{15\,{\rm d}}\right)^{7/3}\right]. \end{aligned} \quad (19)$$

The mass-loss predicted from the semi-analytic model is in good agreement with the simulation results for the retrograde cases (solid lines), which are depicted in Fig. 6 using dot–dashed lines. Our semi-analytic model suggests that in our fiducial model with $\rho_{\rm c} = 10^{-8}\,{\rm g\,cm^{-3}}$, roughly 50 per cent (80 per cent) of the debris mass would be mixed into the disc in 15 d (30 d $\simeq t_0$) while the debris is moving away from the SMBH. Among the rest of the remaining debris (20 per cent), the bound part would have to plow through the disc inwards while it was returning to the SMBH, such that it is very likely that at least the remaining bound debris would be completely mixed into the disc on the way in. In fact, we do not observe any coherent return of debris to the SMBH in our simulations. This means, no TDE-like flare would be generated.

3.3 Energy and angular momentum distribution of debris

In this section, we seek to investigate the energy and energy distribution of debris in AGN discs. Fig. 7 presents the distribution $d^2M/dEdL$ of specific orbital energy E relative to the SMBH and specific angular momentum L of debris for our fiducial models (i.e. $M_\star = 1\,{\rm M}_\odot$ and $\rho_{\rm c} = 10^{-8}\,{\rm g\,cm^{-3}}$). Debris produced in AGN discs undergoes continuous changes in the debris structure, potentially leading to a dramatic modification of the $E - L$ distribution on a relatively short time-scale (e.g. before any of the bound material returns to the SMBH). This continuous evolution of the distribution is one of the main differences between TDEs in AGN discs and those in a vacuum ('naked TDEs'). Not long after the disruption (*left* panel, $t = 0.2$ d), the $L - E$ distribution appears almost identical between the prograde and retrograde cases. However, as the debris travels away from the SMBH, the distribution continuously evolves differently over time, depending on the relative orientation of the orbit. For the prograde case (*top* panels), one of the most noticeable trends is that the angular momentum increases over time. On the other hand, the angular momentum decreases for the retrograde case (*bottom* panels). This trend is expected based on how the motion of the debris is aligned or anti-aligned with the disc flow (see Fig. 5). Additionally, the distribution for the retrograde case is substantially more perturbed by the disc. At around 10 d, most of the debris in the retrograde case is mixed into the disc, and its angular momentum becomes less than 80 per cent of the initial angular momentum. Compared to changes in angular momentum within the debris ($\lesssim 5$ per cent) for naked TDEs (Cheng & Bogdanović 2014; Ryu et al. 2020b), the subsequent change in the angular momentum due to continuous interactions with the disc is much more substantial. Other cases with different disc mid-plane density and stellar masses reveal qualitatively the same trend.

We further present the distribution of E for $M_\star = 1\,{\rm M}_\odot$, by integrating $d^2M/dEdL$ over L, in Fig. 8. Because the energy distribution for the disc with $\rho_{\rm c} \lesssim 10^{-11}\,{\rm g\,cm^{-3}}$ is almost identical to our vacuum case, we only show the distribution for $\rho_{\rm c} \gtrsim 10^{-9}\,{\rm g\,cm^{-3}}$ (also the same for the fallback rate in Section 9). For comparison, we depict the energy distribution of debris produced in a full disruption in a vacuum sharing the same encounter parameters (grey line in each panel), measured at 2 d after disruption. For both prograde (*left* panels) and retrograde (*right* panels) cases, the energy distribution at $t = 0.2$ d is almost identical to that for the naked TDE, except for the sharp cut-off at the far-end of the wing for the unbound debris, indicating that the most unbound debris has been already mixed to the disc. The subsequent interaction of the debris with the disc gas continuously perturbs the debris starting from its head and tails (where the density is the lowest), corresponding to the wings of the distribution. As a result, the distribution becomes narrower. Notice, however, that the rate at which each side of the distribution becomes narrower is different. At early times ($t \lesssim$ a few days), the unbound debris is lost to the disc at a faster rate than the bound debris. However, the 'mixing' or 'slowing-down' rate of the unbound debris becomes slower than that of the bound debris at later times. In all cases except for the retrograde case with $\rho_{\rm c} = 10^{-7}\,{\rm g\,cm^{-3}}$, the distribution for the unbound debris does not change at $t \gtrsim 5$ d, while that for the bound debris continues to shrink. This behaviour can be understood based on when and how long the debris moves in a denser region of the disc. Upon disruption, the unbound debris advances further out, meaning that it interacts with the disc more at a given time. At later times, once the unbound debris moves beyond the density cusp, because the disc density continues to decrease, the perturbation of the unbound debris due to the disc material becomes increasingly weaker. However, the bound debris stays for a longer time in denser parts of the disc as it slows down before returning to the SMBH, meaning more interactions with the disc.

It is worth noting that the distribution becomes bumpy when irregular debris structure develops due to the Rayleigh–Taylor instability, which is more pronounced for the retrograde case with higher disc densities (see the *right* panel of Fig. 5).

The features mentioned above are also found in the cases with different stellar masses. Given the qualitative similarities, we present

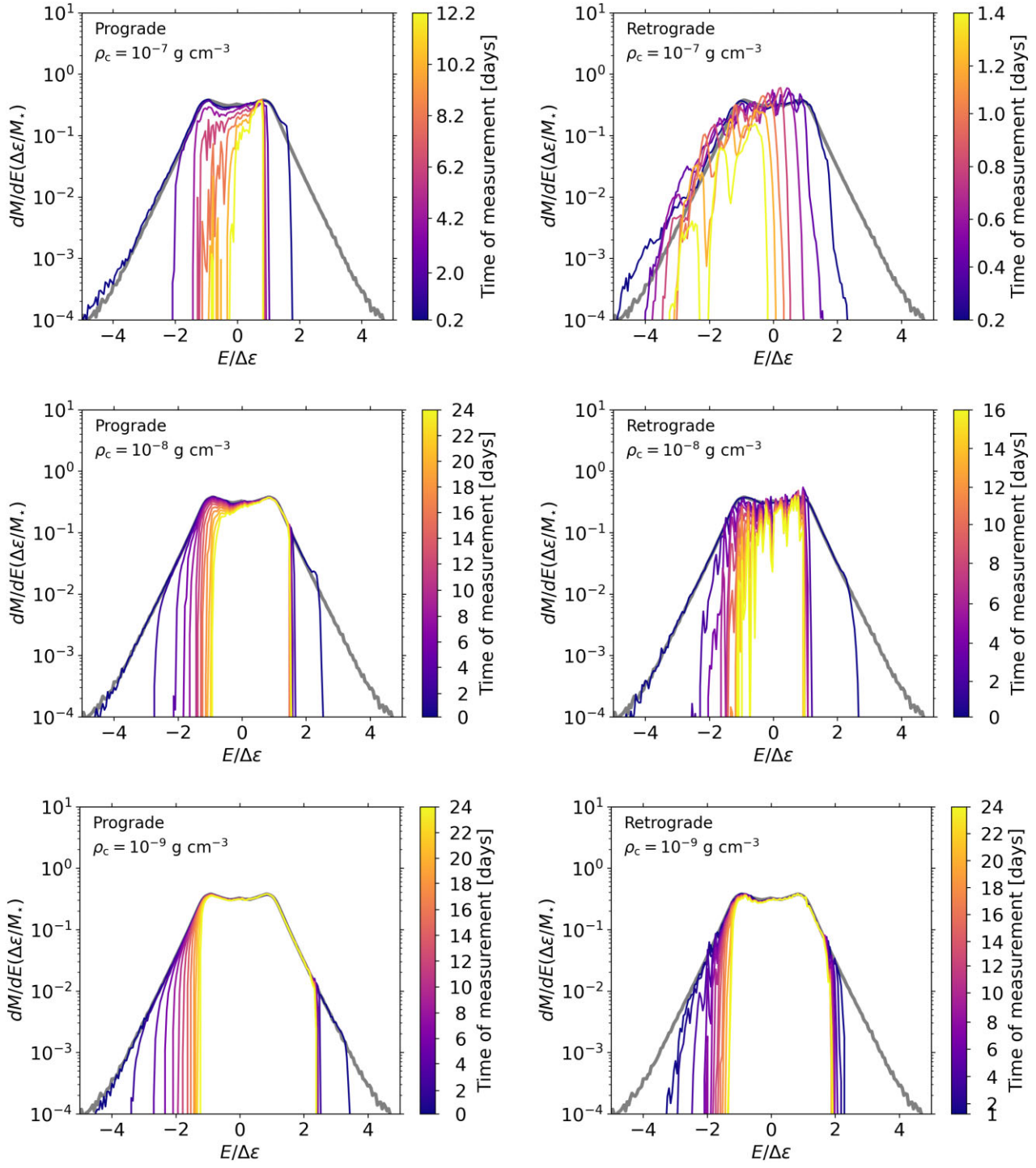

Figure 8. Energy distribution of debris produced in a full disruption of a $1\,M_\odot$ star on a prograde (left) or a retrograde (right) orbit relative to an AGN disc with $\rho_c = 10^{-7}\,g\,cm^{-3}$ (top), 10^{-8}, and $10^{-9}\,g\,cm^{-3}$, around a $10^6\,M_\odot$ SMBH. The grey line in each panel shows TDEs of the same star in vacuum (naked TDEs), which is sitting behind the line for AGN-TDEs at $t \simeq 0$ d. The colour bar indicates the time at which the distribution is measured since disruption. Notice different time-scales in the colour bars.

the distribution for $M_\star = 3$ and $10\,M_\odot$ in the *upper* panels of Figs A1 and A2, respectively. Note that at this pericentre distance, the $3\,M_\odot$ star is only partially disrupted and a remnant survives, which correponds to the peak at $E \simeq 0$ in the energy distribution.

3.4 Fallback rate

Using the energy distribution and assuming a ballistic orbit of the debris, we estimate the mass fallback rate, which is illustrated in Fig. 9 for $M_\star = 1\,M_\odot$. For completeness, we present the fallback rate for $M_\star = 3\,M_\odot$ in Fig. A1 and for $M_\star = 10\,M_\odot$ in Fig. A2.

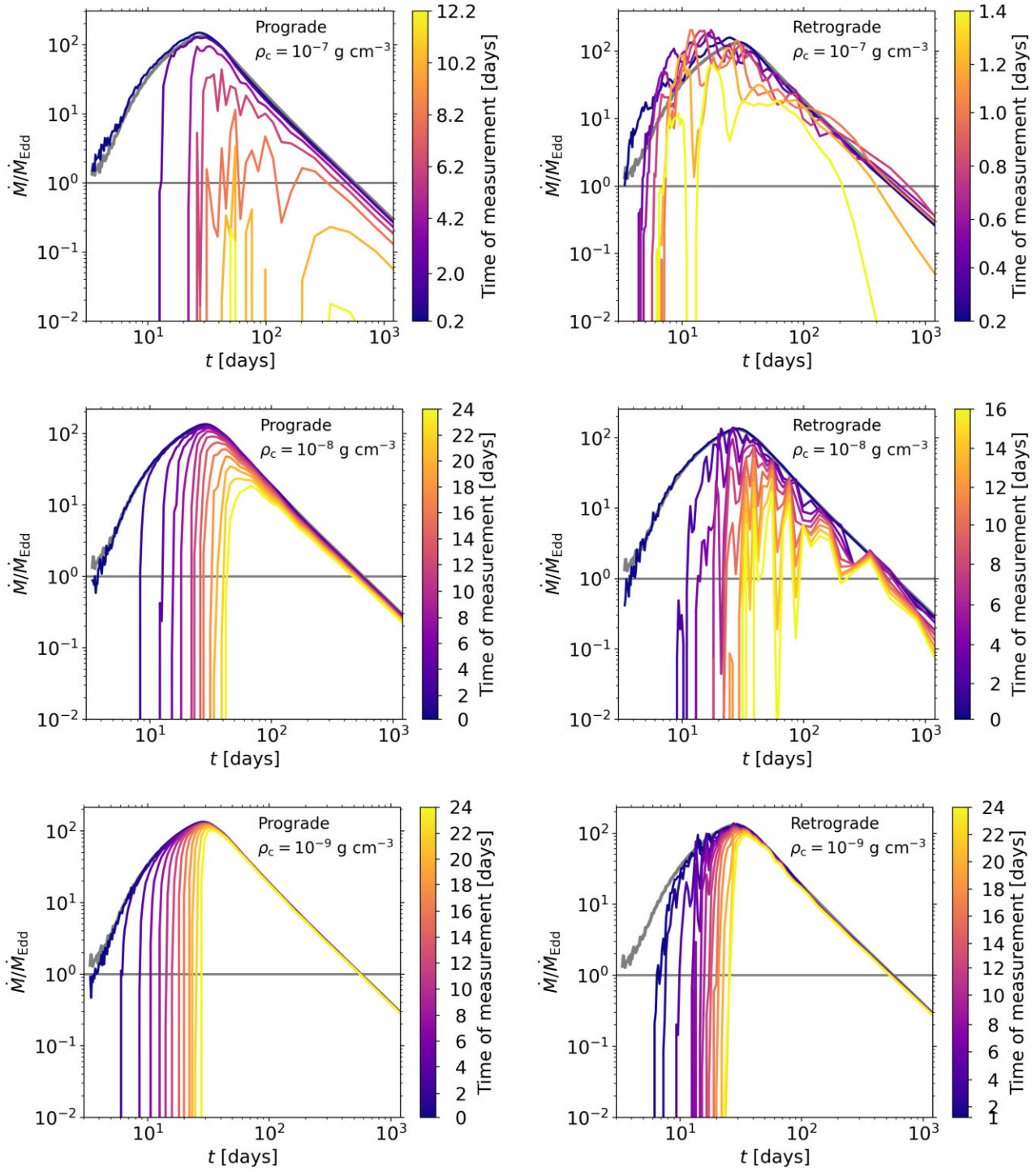

Figure 9. Same as Fig. 8, but for the fallback rate.

The continuous shrinkage of the energy distribution for the bound debris leads to the decrease in the peak fallback rate and increase in the peak fallback time. For $\rho_c = 10^{-8}$ g cm^{-3} with the prograde orbit (*middle-left* panels), the peak mass return rate decreases from $100\dot{M}_{\rm Edd}$ to $20\dot{M}_{\rm Edd}$ in 24 d. Here, $\dot{M}_{\rm Edd} = L_{\rm Edd}/\eta c^2$ where $L_{\rm Edd}$ is the Eddington luminosity with a radiative efficiency $\eta = 0.1$. The debris with a bumpy energy distribution in some of the cases (see Fig. 8 reveals irregular patterns in the rate on top of the trend of the peak fallback rate and time. For example, for $\rho_c = 10^{-8}$ g cm^{-3} (*top* panels), the rate curves gradually shift towards the right-bottom corner of the figure while the curves become increasingly bumpy. The bumpiness and the change in the peak fallback rate and time are greater for higher ρ_c and for a retrograde orbital configuration.

One observationally relevant finding is that *the rate at which the bound debris is mixed into the disc is faster than the rate at which the debris returns in all cases shown in Fig. 9 ($\rho_c \gtrsim 10^{-9}$ g cm^{-3})*. In other words, the bound debris is continuously mixed

into the disc before it returns to the SMBH in a coherent fashion like it does in a naked TDE. This suggests that the resulting light curves of AGN TDEs in sufficiently dense gas discs would not simply be TDE-like light curves on top of AGN light curves (see Section 4.2).

4 DISCUSSION

4.1 Light curves

4.1.1 Passage of star around the SMBH

A close passage of a star can significantly perturb the inner part of the disc, which possibly enhances the accretion rate until the perturbed disc settles again over a time-scale comparable to the cooling time-scale. To zeroth order, whether a stellar passage can significantly affect the structure of the inner disc can be measured by comparing the swept-up mass of the star during the pericentre passage, $M_{\rm swept-up} \simeq \rho_{\rm disc}\pi R_\star^2 r_{\rm p}$, to the disc mass within the pericentre distance, $M_{\rm disc}(r < r_{\rm p}) \simeq \rho_{\rm disc}(h/r)r_{\rm p}^3$,

$$\frac{M_{\rm swept-up}}{M_{\rm disc}(r<r_{\rm p})} = 0.3\left(\frac{h/r}{0.05}\right)^{-1}\left(\frac{M_\star}{10\,{\rm M}_\odot}\right)^{2/3}\left(\frac{M_\bullet}{10^6\,{\rm M}_\odot}\right)^{-2/3}\left(\frac{r_{\rm p}/r_{\rm t}}{0.3}\right)^2. \tag{20}$$

This ratio of order unity suggests that a passage of a main-sequence star, in particular a massive one, can significantly affect the inner disc over a very short time-scale comparable to the dynamical time at pericentre. Qualitatively, this may cause a state-change in the inner disc, much like those observed in changing-look AGN exhibiting an increase in luminosity (Graham et al. 2020). See also Petrushevska et al. (2023) for the TDE candidate PS16dtm that may cause changing look episodes in AGN. The temperature at the innermost stable circular orbit can be parametrized as (McKernan et al. 2022)

$$T_{\rm ISCO} \approx 10^6{\rm K}\left(\frac{M_\bullet}{10^6{\rm M}_\odot}\right)^{-1/4}\left(\frac{\dot{M}}{0.1\dot{M}_{\rm Edd}}\right)^{1/4}\left(\frac{\eta}{0.1}\right)^{-1/4} \times \left(\frac{r_{\rm ISCO}}{6r_g}\right)^{-3/4}\left(\frac{f}{2}\right)^{-1/4}, \tag{21}$$

where $r_{\rm ISCO}$ is the location of the innermost stable circular orbit and f is a numerical factor. By contrast, the temperature of the shock due to the close pass of the star ($T_{\rm shock} \sim L_{\rm shock}/4\pi R_{\rm shock}^2\sigma$) can be parameterized as (McKernan et al. 2022)

$$T_{\rm shock} \approx 4\times10^6{\rm K}\left(\frac{a}{10r_g}\right)^{-3/8}\left(\frac{\rho_{\rm disc}}{10^{-8}{\rm g\,cm^{-3}}}\right)^{1/4}, \tag{22}$$

where we assume $R_{\rm shock} \sim R_\star$ and clearly the passage of the star must heat the innermost disc substantially. At such temperatures, prompt X-ray flaring and fast outflows are likely (e.g. Kosec et al. 2023). If the heating of passage translates into a fiducial local aspect ratio increase then the puffed-up inner disc is accreted on a shorter viscous time-scale t_ν. Since t_ν can be parametrized as (e.g. Stern et al. 2018)

$$t_\nu \sim 6\,{\rm yr}\left(\frac{h/r}{0.05}\right)^{-2}\left(\frac{\alpha}{0.01}\right)^{-1}\left(\frac{M_\bullet}{10^6{\rm M}_\odot}\right)\left(\frac{R}{100r_g}\right)^{3/2}, \tag{23}$$

we can see that e.g. a doubling of average disc aspect ratio h/r due to local heating leads to a significantly shorter (1/4) accretion time-scale and so there is a temporary enhancement in accretion (and therefore $\eta\dot{M}c^2$ luminosity) while the local disc accretes and cools over the approximate thermal time-scale (Stern et al. 2018)

$$t_{\rm th} \sim 12\,{\rm d}\left(\frac{\alpha}{0.01}\right)^{-1}\left(\frac{M_\bullet}{10^6{\rm M}_\odot}\right)\left(\frac{R}{100r_g}\right)^{3/2}. \tag{24}$$

Thus, if debris from the TDE can make it back to the SMBH on these time-scales ($t_{\rm th}$), the initial impulse heating is continued and added to, in a single episode. If debris from the TDE takes longer than $t_{\rm th}$ to return to the inner disc, then the light curve will consist of two separate episodes, the initial perturbation, followed by the debris fallback and accretion. But as explained in the following section, the TDE-like light curves from the debris fallback and accretion can only be created when the disc density is sufficiently small.

4.1.2 Full tidal disruption event

The subsequent source of a flare is the stellar debris produced in the tidal disruption. The biggest difference between in-plane AGN TDEs and 'naked' or standard TDEs is the continuous interaction between debris and disc gas, resulting in the time evolution of the debris orbits and debris structure. In naked TDEs, because the debris' orbit is almost ballistic, the post-disruption debris orbit does not change significantly over time until debris returns to the SMBH. This feature allows us to make a prediction for the fallback rate curve (Hills 1988; Rees 1988) with the energy distribution of debris upon disruption. However, in the case of AGN-TDEs, because the debris continuously interacts with surrounding disc gas, the shape of the fallback rate curve, such as the peak fallback rate and the slope of the decaying part of the fallback rate curve, depends strongly on the disc density ($\rho_{\rm disc}$). If $\rho_{\rm disc}$ is sufficiently high, greater than some critical value ($\rho_{\rm crit}$), the debris is completely mixed with the disc before it ever returns. In this case, no debris returns to the SMBH in a coherent and eccentric fashion as predicted for naked TDEs.

Using the semi-analytic model developed in Section 3.2 we estimate $\rho_{\rm crit}$ for a complete dissociation of the debris in a retrograde orbit on a time-scale comparable to the peak mass return time (estimated assuming naked TDEs) as a function of $M_\star$ and $M_\bullet$ in the *left* panel of Fig. 10. Although we assume $r_{\rm cusp} = 10^3 r_{\rm g}$ here, $\rho_{\rm crit}$ can be easily calculated using our semi-analytic model (see Section 3.2) with different values of $r_{\rm cusp}$. As shown in the *left* panel, the minimum $\rho_{\rm crit}$ has a relatively weak dependence on $M_\star$ while it mostly depends on $M_\bullet$. The reason that $\rho_{\rm crit}$ is lower for higher $M_\bullet$ is because each part of the debris travels a longer absolute distance for a given peak mass return time. We also present in the *right* panel the ratio of the time for a complete dissociation $t_{\rm dis} = t(M_{\rm d} = M_\star)$ of debris to the peak mass return time t_0 for naked TDEs as a function of $\rho_{\rm crit}$ and $M_\bullet$, suggesting that in the large parameter space relevant for AGN discs, debris is completely mixed with the disc before returning to the SMBH. Thus, for dense AGN discs, *the resulting light curves cannot be described by a simple superposition of the luminosity of naked TDEs on top of that of AGN discs*. Conveniently, we can parametrize $\rho_{\rm crit}$ at $t_{\rm dis} \simeq t_0$ for the retrograde TDEs, as

$$\rho_{\rm crit} \simeq 10^{-8}{\rm g\,cm^{-3}}\left(\frac{M_\bullet}{10^6\,{\rm M}_\odot}\right)^{-2.5}. \tag{25}$$

The value of $\rho_{\rm crit}$ would be higher for prograde TDEs than that for retrograde TDEs. Even for those cases where the debris is partially disintegrated, because the mass fallback rate curve would be significantly different from that for naked TDEs, the resulting luminosity associated with the disruption of a star could be different. Nonetheless, the returned debris can perturb the inner disc, which would boost the luminosity temporarily. However, detailed modelling of the response of the disc near the SMBH is beyond the scope of this paper.

In some cases, disruptions end up adding some mass to the disc without generating a TDE-like flare. However the addition of the

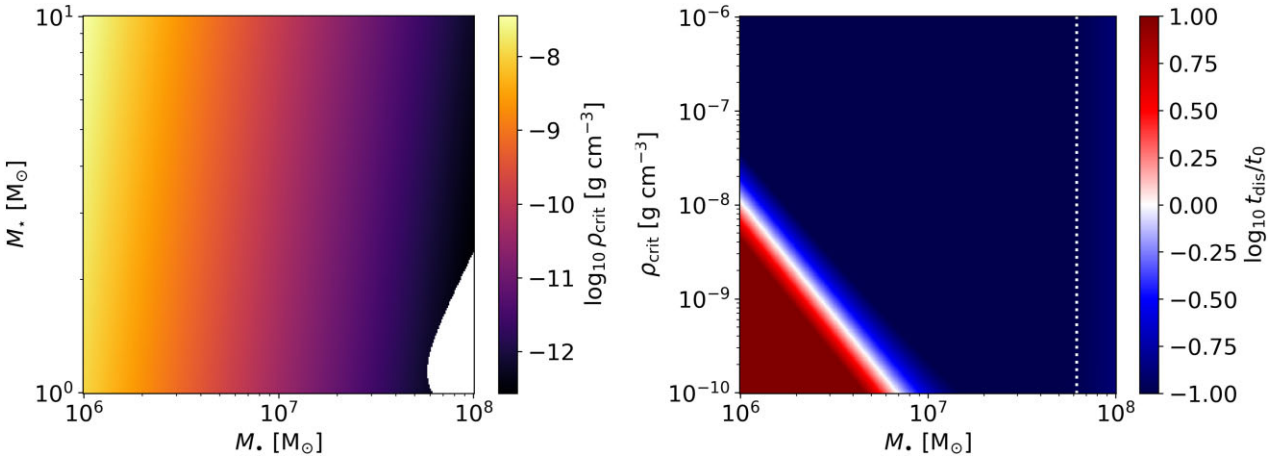

Figure 10. The minimum critical density $\rho_{\rm crit}$ (left) above which the entire debris is completely mixed into the disc on the peak mass return time t_0 estimated right after disruption in a $M_\star - M_\bullet$ plane and the ratio of the complete dissociation time $t_{\rm dis}$ to the peak mass return time in a $\rho_{\rm crit} - M_\bullet$ plane. Here, t_0 is estimated by including the correction factor for the stellar internal structure and relativistic effects (Ryu et al. 2020a, b, c, d). The white region near the corner indicates the region of parameter space where stars would be directly captured by the black hole. Similarly, the vertical dashed white line indicates the maximum black hole mass for direct captures.

mass would have a minimal effect on the disc structure because the disc mass inside the radius at which the debris is completely disintegrated, namely $r \gtrsim 10^3 r_{\rm g}$ for $\rho_{\rm c} \lesssim 10^{-7}$g cm^{-3}, is much greater than the mass of the debris (see Fig. 6).

Quantitatively, in the limit of low $\rho_{\rm disc} \ll \rho_{\rm c}$ (more specifically $\rho_{\rm disc} \lesssim \rho_{\rm c}/10^3$ based on our simulations), AGN-TDEs should look increasingly like standard 'naked' TDEs. Thus, observations of a TDE-like light curve in an AGN should indicate a low-density disc with $\rho_{\rm disc} \ll \rho_{\rm c}$. A low-density disc at large radii might be responsible for late-time radio signatures years post-TDE (Cendes et al. 2022), as part of the debris that would otherwise escape interacts with the gas disc and returns later than the main apparently 'naked' TDE. Thus late-time responses to otherwise 'naked' TDEs could indicate either a weak AGN, or a more distant fuel reservoir, interacting with the debris, driving much later material return.

4.1.3 Partial tidal disruption event

The source of AGN-TDEs are embedded stars that have either been scattered via dynamical encounters into the AGN loss cone, or on highly eccentric orbits. In both cases, the probability of a partial tidal disruption event (where pericentre passage of the star is close, but not too close, to the SMBH) should be higher than an actual AGN-TDE. It is worth considering the observational implications of partial AGN-TDEs.

As we have seen above, AGN-TDE debris mixing can be significant, particularly in dense AGN discs. This can inhibit and, if the disc is dense enough ($\rho_{\rm disc} > \rho_{\rm crit}$), completely prevent the return of TDE material to the SMBH. However, in the case of a partial disruption, some of the outer part of the star is stripped, but the core remains coherent. As long as the orbit is bound (e.g. if the orbit is highly eccentric), it should return to the SMBH on approximately the orbital period, $T_{\rm orb} \sim 5\,{\rm d}(a/600r_{\rm g})^{3/2}(M_\bullet/10^6\,{\rm M}_\odot)$ where a is the semimajor axis of the remnant's orbit. Repeated passage of a bound remnant will generate similar heating of the inner disc to the first pericentre passage. Such partial disruption perturbations could yield transients like quasi-periodic eruptions (QPEs) as observed in X-rays in some AGNs around low mass SMBHs (e.g. Wevers et al. 2022). The magnitude of any repeating flare depends on the remnant mass and the ratio of the local thermal time-scale ($t_{\rm th}$) to the returning time-scale ($T_{\rm orb}$ in this case). For example, if the remnant mass is smaller and $t_{\rm th} > T_{\rm orb}$, the heating flare will appear less prominent against a higher AGN continuum state. In order to explain observed QPE time-scales of O(day), this would require highly eccentric retrograde stellar orbits at $a \sim$ few $\times\ 10^2 r_{\rm g}$, around smaller mass SMBHs. Such orbits may occur early on in the AGN phase due to disc capture (Wang, Zhu & Lin 2023) or rapid retrograde orbital decay (McKernan et al. 2022).

4.2 Metallicity of AGN discs

AGNs are generally believed to have high metallicity. In particular the broad-line region metallicity in AGNs is observed to be substantially super-solar out to high redshift (Hamann & Ferland 1999; Juarez et al. 2009). Quasar host galaxies at $z < 2$ are surrounded by metal-enriched cool gas, believed to originate in AGN outflows (Prochaska, Hennawi & Simcoe 2013). Of course some of this metallicity enrichment could come from supernovae embedded in AGN at a rate of $O(10^{-4}){\rm yr}^{-1}$ (Juarez et al. 2009), a rate which is very similar to the expected standard TDE rate. It is unclear how stars embedded in AGN discs evolve; but it is possible that they do not undergo supernovae but instead grow in mass and support themselves by inflow of fresh hydrogen from the AGN disc (Cantiello, Jermyn & Lin 2021; Jermyn et al. 2023). If this occurs non-negligibly often, then supernovae would be more rare in AGNs than naively expected from standard stellar evolution, making TDEs a plausible means of enriching AGN metallicity. TDEs can also occur around stellar mass BH embedded in AGN discs, yielding micro-TDEs (Perets et al. 2016; Yang et al. 2022). Such micro-TDEs can also contribute to metallicity enhancement in the disc.

Assuming TDEs are the sole source of metallicity enhancement through the mixing of stellar debris with the disc, one can estimate, to an order of magnitude, the number of AGN-TDEs, denoted by $N_{\rm TDE}$, of stars with metallicity $Z_\star > Z_1$ required to elevate the metallicity of the AGN disc from Z_0 to Z_1. The total enclosed mass of the disc within a distance at which a fractional mass ξ of the debris is mixed

after $N_{\rm TDE}$ TDEs is $\xi N_{\rm TDE} M_\star + M_{\rm disc}$ and the total mass of metals after TDEs $Z_0 M_{\rm disc} + Z_\star \xi N_{\rm TDE} M_\star$. Assuming the total enclosed mass of the disc is conserved, $N_{\rm TDE}$ can be expressed as,

$$N_{\rm TDE} = \left(\frac{Z_1 - Z_0}{Z_\star - Z_1}\right)\left(\frac{M_{\rm disc}}{\xi M_\star}\right), \quad (26)$$

where $M_{\rm disc}$ is the enclosed mass of the disc into which debris with a mass of $\xi M_\star$ is mixed. As an example, to enhance the metallicity from $Z_2 \simeq 0.1 Z_\odot$ to $Z_1 \simeq 0.9 Z_\odot$ through TDEs of 1 $M_\odot$ stars, $N_{\rm TDE} \simeq 1000\xi^{-1}(M_{\rm disc}/10^2\,{\rm M}_\odot)(M_\star/\,{\rm M}_\odot)^{-1}$ when $Z_\star = Z_\odot$. If $Z_\star = 2Z_\odot$, $\simeq 100\xi^{-1}(M_{\rm disc}/10^2\,{\rm M}_\odot)(M_\star/\,{\rm M}_\odot)^{-1}$.

However, it is important to note that many variables, namely $M_\star$, $Z_\star$, $M_{\rm disc}$, and ξ, are highly uncertain. To determine these quantities accurately, a more detailed modelling of the dynamics in stellar clusters around AGN discs would be necessary.

5 CAVEATS

Although our simulations treat hydrodynamical effects accurately, there are two main caveats. First, no relativistic effects are included. It has been recognized that relativistic effects would play a major role in determining the evolution of debris in TDEs by massive black holes (e.g. Bonnerot & Stone 2021). This would be applicable to in-plane TDEs in AGN discs with low disc densities. However, if the disc density is sufficiently high so that the debris is mixed before its return, relativistic effects on the long-term evolution of debris would be irrelevant. However, because debris would stay a longer time near pericentre, it is possible that the perturbation of the inner disc at the first pericentre passage would be stronger for more relativistic cases (e.g. extremely relativistic TDEs; Ryu et al. 2023). Second, we do not include radiation pressure in our simulations. The standard AGN disc model suggests that the inner part of the disc is radiation pressure-dominated (Shakura & Sunyaev 1973; Sirko & Goodman 2003). Because our disc is supported only by the gas pressure, the temperature is significantly higher than the case where the disc is supported both by the radiation and gas pressure. We will investigate the impact of radiation pressure on the disc temperature profile and how this in turn affects the time evolution of the debris in a follow-up project.

6 SUMMARY AND CONCLUSIONS

In this work, we investigated the evolution of debris in tidal disruption events of main-sequence stars by a $10^6\,{\rm M}_\odot$ supermassive black hole, surrounded by a gaseous disc, using the moving-mesh hydrodynamics simulation code AREPO. We consider three stellar masses, $M_\star = 1$, 3, and $10\,{\rm M}_\odot$, and a range of mid-plane maximum disc densities $\rho_{\rm c} = 10^{-12}$–$10^{-7}\,{\rm g\,cm^{-3}}$.

The results of the simulations can be summarized as follows,

(i) Stellar debris produced in an in-plane disruption in an AGN disc is continuously perturbed by the disc gas as it plows through the disc. As a result, the energy and angular momentum of the debris evolves differently over time relative to TDEs in a vacuum. For prograde TDEs (those of stars on a prograde orbit relative to the disc orbit), the debris' angular momentum increases whereas the debris' angular momentum decreases for retrograde TDEs.

(ii) For a sufficiently high-disc density, a large fraction of the debris can be disintegrated and mixed into the disc via the interaction with the disc. The mixing is more significant for retrograde TDEs. This gradual mixing is a unique feature that is clearly distinguished from tidal disruption events in a vacuum.

(iii) For high-density AGN discs, it is likely that the debris produced in retrograde TDEs is fully mixed into the disc before any of the debris material returns in a coherent fashion as in naked TDEs. The critical density above which the retrograde debris is completely mixed into the disc on a time-scale comparable to the peak mass return time for naked TDEs is $\rho_{\rm crit} \sim 10^{-8}{\rm g\,cm^{-3}}(M_\bullet/10^6\,{\rm M}_\odot)^{-2.5}$. Note that this critical density is the minimum density of disintegration of the entire debris. The density above which no bound material returns to the SMBH would be lower, $\rho_{\rm crit,bound} \sim 10^{-9}{\rm g\,cm^{-3}}(M_\bullet/10^6\,{\rm M}_\odot)^{-2.5}$. Even for prograde TDEs, no coherent fallback has been found when the maximum disc density is $\geq 10^{-9}\,{\rm g\,cm^{-3}}$.

(iv) The mixing of the stellar material into the disc has several astrophysical implications. First, the light curves of in-plane TDEs in an AGN disc, whose density is high enough to cause the disintegration of the debris, could be significantly different from just the superposition of light curves of naked TDEs on top of those of AGN discs. A first burst should originate from the close passage of a star, perturbing and heating up the inner part of the disc, possibly resulting in an enhancement of the accretion rate until the perturbed disc settles on the local thermal time-scale ($t_{\rm th}$). Thus we expect an observable state-change in the AGN emission from a close passage, similar to that observed in changing-look AGN, with significant X-ray flaring around smaller mass SMBHs. At low-density ($\rho_{\rm disc} \lesssim \rho_{\rm crit,bound}/10^2$), the gas reservoir at moderately large distances from the SMBH ($>10^4 r_{\rm g}$) might generate late-time debris return and account for recent *very* late-time signatures of (otherwise naked) TDEs (e.g. Cendes et al. 2022). At modest disc densities ($\rho_{\rm crit,bound}/10^2 < \rho < \rho_{\rm crit,bound}$), AGN TDE debris is only partially mixed and the rest returns, generating a secondary, longer, inner disc flaring episode via both inner disc perturbation as well as accretion of debris. At high disc densities ($\rho_{\rm disc} \geq \rho_{\rm crit,bound}$) no TDE-like light curves are created, past the initial state-change, but a mildly elevated accretion rate (and higher luminosity) should persist for years due to the complete mixing of debris.

(v) For partial disruptions, recurring passage of the stellar remnant will heat the inner disc, creating recurring flares. A population of highly eccentric retrograde orbiters around low mass SMBHs should produce QPEs in X-rays from partial AGN TDEs. Whether each flare is separate or the disc response is blended depends on the orbital period of the embedded partially disrupted star as well as disc properties. Short time-scale QPEs are therefor a test of both the population of eccentric retrograde orbiters and the AGN disc.

(vi) The mixing of the stellar debris in AGN TDEs contributes to the enhancement of the disc metallicity. Supernovae of stars embedded in a disc could be another source of metallicity enhancement. But if stars grow in mass without undergoing supernovae, mixing from AGN TDEs (and micro-TDEs) could be an important mechanism to elevate disc metallicity.

Identifying such events in a large sample of AGN can provide a constraint on typical densities of AGN discs and the embedded stellar population while the disc exists which are otherwise are hard to probe. Going forward, it will be imperative to understand the shape of the light curves that account for the passage of the star and the evolution of debris as a function of disc density. It will also be important to track returning masses in the case of partial AGN TDEs, to test models of QPEs in AGN around low-mass SMBHs. In order to investigate the contribution of AGN TDEs to the evolution of metallicity enhancements in AGN discs, detailed modelling of the dynamics between stellar-mass objects in nuclear star clusters

surrounding AGN discs would be required over a cosmological timescale.

ACKNOWLEDGEMENTS

The authors are grateful to the anonymous referee for carefully reviewing the manuscript. TR is very grateful to Max Gronke for a useful discussion for the mixing of gas. This research project was conducted using computational resources (and/or scientific computing services) at the Max-Planck Computing & Data Facility. The authors gratefully acknowledge the scientific support and HPC resources provided by the Erlangen National High Performance Computing Center (NHR@FAU) of the Friedrich-Alexander-Universität Erlangen-Nürnberg (FAU) under the NHR project b166ea10. NHR funding was provided by federal and Bavarian state authorities. NHR@FAU hardware was partially funded by the German Research Foundation (DFG) – 440719683. In addition, some of the simulations were performed on the national supercomputer Hawk at the High Performance Computing Center Stuttgart (HLRS) under the grant number 44232. BM & KESF were supported by NSF AST-2206096 and NSF AST-1831415 and Simons Foundation Grant 533845, with additional sabbatical support from the Simons Foundation. NWCL gratefully acknowledges the generous support of a Fondecyt General grant 1230082, as well as support from Millenium Nucleus NCN19_058 (TITANs) and funding via the BASAL Centro de Excelencia en Astrofisica y Tecnologias Afines (CATA) grant PFB-06/2007. NWCL also thanks support from ANID BASAL project ACE210002 and ANID BASAL projects ACE210002 and FB210003.

DATA AVAILABILITY

Any data used in this analysis are available on reasonable request from the first author.

REFERENCES

Artymowicz P., Lin D. N. C., Wampler E. J., 1993, ApJ, 409, 592
Bondi H., 1952, MNRAS, 112, 195
Bondi H., Hoyle F., 1944, MNRAS, 104, 273
Bonnerot C., Stone N. C., 2021, Space Sci. Rev., 217, 16
Cantiello M., Jermyn A. S., Lin D. N. C., 2021, ApJ, 910, 94
Cendes Y. et al., 2022, ApJ, 938, 28
Chan C.-H., Piran T., Krolik J. H., 2021, ApJ, 914, 107
Cheng R. M., Bogdanović T., 2014, Phys. Rev. D, 90, 064020
Coughlin E. R., Nixon C., Begelman M. C., Armitage P. J., 2016, MNRAS, 459, 3089
Dutta A., Sharma P., 2019, Res. Notes Am. Astron. Soc., 3, 148
Fabj G., Nasim S. S., Caban F., Ford K. E. S., McKernan B., Bellovary J. M., 2020, MNRAS, 499, 2608
Farber R. J., Gronke M., 2022, MNRAS, 510, 551
Farber R. J., Ruszkowski M., Tonnesen S., Holguin F., 2022, MNRAS, 512, 5927
Generozov A., Perets H. B., 2023, MNRAS, 522, 1763
Goodman J., Tan J. C., 2004, ApJ, 608, 108
Graham M. J. et al., 2020, MNRAS, 491, 4925
Gronke M., Oh S. P., 2018, MNRAS, 480, L111
Hamann F., Ferland G., 1999, ARA&A, 37, 487
Hills J. G., 1988, Nature, 331, 687
Jermyn A. S. et al., 2023, ApJS, 265, 15
Jermyn A. S., Dittmann A. J., McKernan B., Ford K. E. S., Cantiello M., 2022, ApJ, 929, 133
Juarez Y., Maiolino R., Mujica R., Pedani M., Marinoni S., Nagao T., Marconi A., Oliva E., 2009, A&A, 494, L25
Kanjilal V., Dutta A., Sharma P., 2021, MNRAS, 501, 1143
Kosec P., Pasham D., Kara E., Tombesi F., 2023, ApJ, 954, 170
Lee A. T., Stahler S. W., 2011, MNRAS, 416, 3177
Lee A. T., Stahler S. W., 2014, A&A, 561, A84
Leigh N. W. C. et al., 2018, MNRAS, 474, 5672
Levin Y., 2007, MNRAS, 374, 515
McCourt M., O'Leary R. M., Madigan A.-M., Quataert E., 2015, MNRAS, 449, 2
McKernan B., Ford K. E. S., Cantiello M., Graham M., Jermyn A. S., Leigh N. W. C., Ryu T., Stern D., 2022, MNRAS, 514, 4102
Monaghan J. J., Lattanzio J. C., 1985, A&A, 149, 135
Nasim S. S. et al., 2023, MNRAS, 522, 5393
Nelson R. P., Gressel O., Umurhan O. M., 2013, MNRAS, 435, 2610
Neumayer N., Seth A., Böker T., 2020, A&AR, 28, 4
Ohlmann S. T., Röpke F. K., Pakmor R., Springel V., 2017, A&A, 599, A5
Pakmor R., Springel V., Bauer A., Mocz P., Munoz D. J., Ohlmann S. T., Schaal K., Zhu C., 2016, MNRAS, 455, 1134
Paxton B. et al., 2013, ApJS, 208, 4
Paxton B. et al., 2015, ApJS, 220, 15
Paxton B. et al., 2019, ApJS, 243, 10
Paxton B., Bildsten L., Dotter A., Herwig F., Lesaffre P., Timmes F., 2011, ApJS, 192, 3
Perets H. B., Li Z., Lombardi James C. J., Milcarek Stephen R. J., 2016, ApJ, 823, 113
Petrushevska T. et al., 2023, A&A, 699, A140
Prochaska J. X., Hennawi J. F., Simcoe R. A., 2013, ApJ, 762, L19
Rayleigh, 1882, Proc. London Math. Soc., 14, 170
Rees M. J., 1988, Nature, 333, 523
Ryu T., Krolik J., Piran T., Noble S. C., 2020a, ApJ, 904, 98
Ryu T., Krolik J., Piran T., Noble S. C., 2020b, ApJ, 904, 99
Ryu T., Krolik J., Piran T., Noble S. C., 2020c, ApJ, 904, 100
Ryu T., Krolik J., Piran T., Noble S. C., 2020d, ApJ, 904, 101
Ryu T., Perna R., Pakmor R., Ma J.-Z., Farmer R., de Mink S. E., 2023, MNRAS, 519, 5787
Secunda A., Hernandez B., Goodman J., Leigh N. W. C., McKernan B., Ford K. E. S., Adorno J. I., 2021, ApJ, 908, L27
Shakura N. I., Sunyaev R. A., 1973, A&A, 24, 337
Sirko E., Goodman J., 2003, MNRAS, 341, 501
Springel V., 2005, MNRAS, 364, 1105
Springel V., 2010, MNRAS, 401, 791
Stern D. et al., 2018, ApJ, 864, 27
Stone N. C., Vasiliev E., Kesden M., Rossi E. M., Perets H. B., Amaro-Seoane P., 2020, Space Sci. Rev., 216, 35
Taylor G., 1950, Proc. R. Soc., 201, 192
Wang Y.-H., McKernan B., Ford S., Perna R., Leigh N. W. C., Mac Low M.-M., 2021, ApJ, 923, L23
Wang Y., Zhu Z., Lin D. N. C., 2023, preprint (arXiv:2308.09129)
Weinberger R., Springel V., Pakmor R., 2020, ApJS, 248, 32
Wevers T., Pasham D. R., Jalan P., Rakshit S., Arcodia R., 2022, A&A, 659, L2
Yang Y., Bartos I., Fragione G., Haiman Z., Kowalski M., Márka S., Perna R., Tagawa H., 2022, ApJ, 933, L28

APPENDIX A: ENERGY DISTRIBUTION AND FALLBACK RATE FOR DIFFERENT STELLAR MASSES

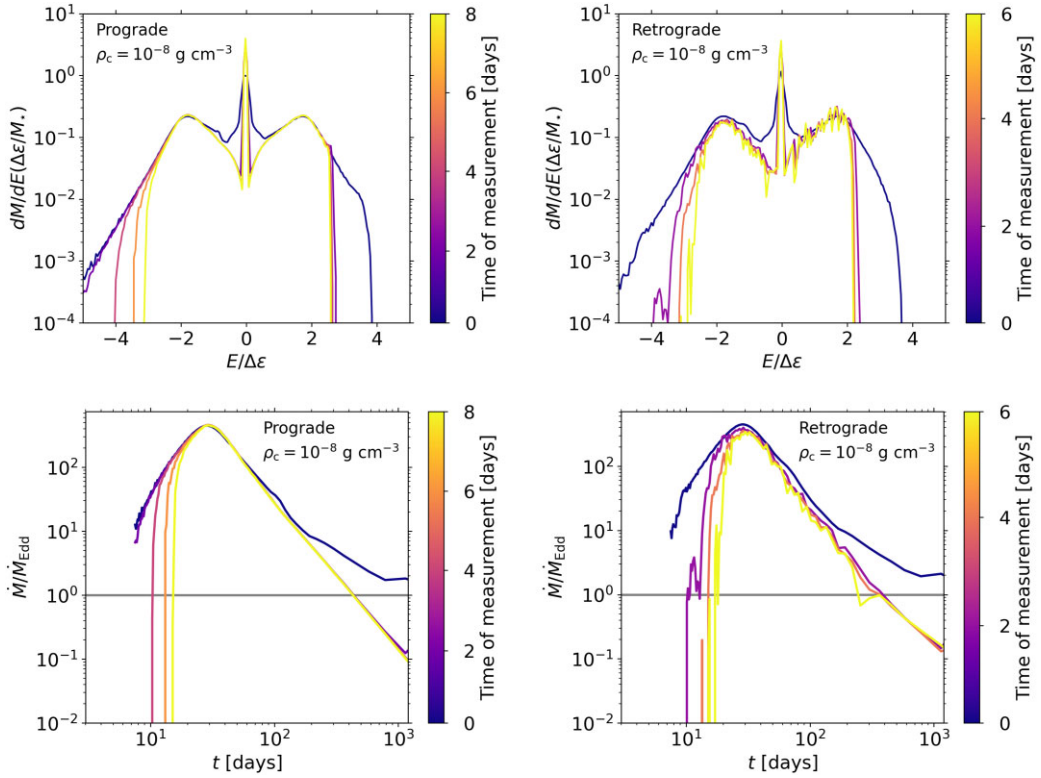

Figure A1. Energy distribution (top) and fallback rate (top) for $M_\star = 3\,\mathrm{M}_\odot$ on a prograde (left) and retrograde (right) orbit. Note that the peak of the distribution at $E \simeq 0$ indicates that a remnant survives after disruption.

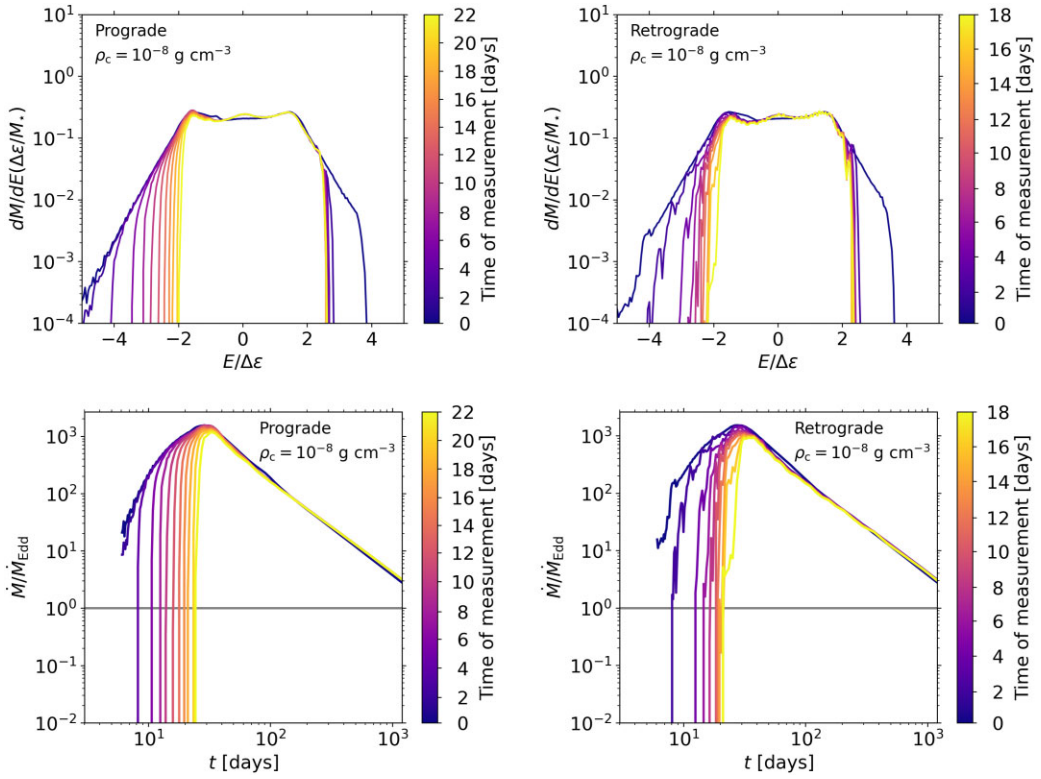

Figure A2. Same as Fig. A1, but for $M_\star = 10\,\mathrm{M}_\odot$.

This paper has been typeset from a TEX/LATEX file prepared by the author.